J MATER SCI 41 (2006) 2259–2270

Investigation of high-temperature plastic deformation using instrumented microindentation tests. Part I *The deformation of three aluminum alloys at 473 K to 833 K*

V. BHAKHRI, R. J. KLASSEN*
Department of Mechanical and Materials Engineering, Faculty of Engineering, University of Western Ontario, London, Ontario, N6A 5B9, Canada

Published online: 22 April 2006

Constant-load indentation tests were performed on wrought-2024, P/M-2024, and wrought-1100 aluminum alloys to assess the capability of the microindentation testing technique for measuring the high-temperature deformation rate controlling parameters of these alloys. The three alloys all display threshold indentation stress σ_{th} below which the indentation strain rate $\dot{\varepsilon}_{ind}$ approaches zero. The nominal inter-obstacle spacing, ℓ^*, calculated from σ_{th}, increases with temperature in a way that is consistent with the known temperature dependence of the inter-particle spacing and dislocation cell size. The measured activation energy ΔG_o of $\dot{\varepsilon}_{ind}$ increases with temperature but remains within the range that is typical of deformation that occurs by dislocation glide limited by weak particles or dislocation/dislocation interactions. The three alloys tested show different trends of ΔG_o versus ℓ^* and the trends are consistent with the known temperature dependence of the obstacles to dislocation glide.

This study demonstrates that high-temperature indentation tests are sufficiently precise to detect changes in the operative deformation parameters between different alloys of the same general composition. This lays the groundwork for the use of this technique as a general tool for studying the local high-temperature deformation of a wide range of metal-based systems.

1. Introduction

Micro-indentation tests performed with pyramidal indenters under constant indentation load conditions have been used for many years to measure characteristics of the time-dependent plastic deformation of materials [1–13]. Interpretation of the dependence of the average indentation strain rate $\dot{\varepsilon}_{ind}$ upon the average indentation stress σ_{ind} and the temperature is difficult because of the complex distribution of stress around the indentation. Many of the past investigators [5–12] have invoked the assumption of a steady-state indented microstructure to interpret the observed dependence of $\dot{\varepsilon}_{ind}$ upon σ_{ind} and T. High-temperature pyramidal indentation creep tests performed on ductile metals have shown that this assumption is largely inconsistent with the measured data since both the apparent power-law dependence of $\dot{\varepsilon}_{ind}$ upon σ_{ind} and the apparent thermal activation energy of $\dot{\varepsilon}_{ind}$ are usually much larger than what would be expected if the deformation were to occur by a steady-state climb-limited dislocation glide process. This is despite the fact that such a process is known to operate during constant uniaxial stress creep of these metals. This finding is not surprising since the local indentation stress state is nonuniform and decreases continuously with time: Moreover, indentation creep tests are of shorter time duration than conventional constant uniaxial stress tests.

Li *et al.* [6] have demonstrated that much of the published indentation creep data from such tests can best be described in terms of deformation by the mechanism of dislocation glide limited by discrete obstacles. The shear strain rate $\dot{\gamma}$ resulting from such a deformation mechanism

*Author to whom all correspondence should be addressed.
0022-2461
DOI: 10.1007/s10853-006-7174-7

when operating under a constant uniaxial shear stress is expressed as

$$\dot{\gamma} = \dot{\gamma}_0 e^{\frac{-\Delta G(\tau)}{kT}} \tag{1}$$

where $\dot{\gamma}_0$ is a material constant, of the order 10^6 $\sec^{-1}$ [14], $\Delta G(\tau)$ is the thermal energy required for a dislocation to overcome an obstacle, and k and T have the usual values. The form of this equation does not presuppose steady-state deformation since $\Delta G(\tau)$ is variable; under steady-state deformation conditions, ΔG becomes constant. Other researches have used Equation 1 to describe the strain-rate sensitivity of σ_{ind} during room-temperature indentation of several common ductile metals [15–18].

The average indentation stress, for mechanically isotropic metals, can be related to an equivalent indentation shear stress as [6]

$$\tau_{\text{ind}} = \frac{\sigma_{\text{ind}}}{3\sqrt{3}} \tag{2}$$

where σ_{ind} is defined as the indentation force/the projected area of the indentation. The nominal equivalent indentation shear strain rate can be expressed, for this type of material, in terms of the indentation depth h and velocity $\dot{h}$ as

$$\dot{\gamma}_{\text{ind}} = \sqrt{3}\dot{\varepsilon}_{\text{ind}} = \sqrt{3}\frac{\dot{h}}{h} \tag{3}$$

An indentation test performed at high temperature with a pyramidal shaped indenter subjected to constant indentation force will display decreasing $\dot{\gamma}_{\text{ind}}$ and τ_{ind} with increasing time. Equations 2 and 3 allow the data from such tests to be applied to Equation 1 to determine $\Delta G(\tau)$. The resulting plot of $\Delta G(\tau)$ versus τ_{ind} depicts the dislocation-obstacle interactions that govern the indentation strain rate. These interactions could change in strength and spacing, and hence ΔG could change, while the indented microstructure evolves in the early stages of the indentation tests. The $\Delta G(\tau)$ versus τ_{ind} profile will reflect this evolution.

A characteristic feature of constant-load pyramidal indentation creep tests is that they display a threshold indentation stress σ_{th} below which $\dot{\varepsilon}_{\text{ind}}$ becomes immeasurably small. Differences in σ_{th} between the materials, tested with the same indenter geometry at the same h, will indicate differences in the deformed microstructure. The microstructural factors that influence σ_{th} are related to the strength and spacing of the discrete obstacles that limit the dislocation glide process.

We report here the results of a study of the dependence of σ_{th} upon T and the dependence of $\dot{\varepsilon}_{\text{ind}}$ upon σ_{ind} and T of three aluminum alloys tested over the temperature range from 473 to 833 K. The alloys are of different chemical compositions and fabrication routes. The objective of the study is to determine if high-temperature constant-load pyramidal indentation is sufficiently precise to detect differences in the microstructural parameters that govern the time-dependent deformation of three different aluminum alloys.

TABLE I Chemical composition and average grain diameter of the P/M 2024, Wrought 2024 and Wrought 1100 Al alloys

Elements	P/M 2024 Al (wt.%)	Wrought 2024 Al (wt.%)	Wrought 1100 Al (wt.%)
Cu	4	3.8 – 4.9	0.05 – 0.2
Mg	1.4	1.2 – 1.8	–
Mn	0.4	0.3 – 0.9	0.05
Fe	–	0.5	0.5
Zn	–	0.25	0.1
Si	–	0.5	0.5
Ti	–	0.15	–
Cr	–	0.1	–
Al	Bal.	Bal.	Bal.
Average grain diameter (± 1 stand. Dev.)	8.5 ± 1.1 μm	8.6 ± 3.7 μm	93.6 ± 13.3μm

2. Procedure

This study was performed on three aluminum alloys; one of 1100 composition and two of 2024 composition (Table I). The 1100 alloy and one of the 2024 alloys were fabricated by conventional liquid metal-based techniques. We refer to these as the wrought aluminum alloys. The second 2024 alloy was fabricated by a solid-state Powder Metallurgy (P/M) technique [19]. We refer to this as the P/M aluminum alloy. These alloys were chosen for this investigation because their microstructure is very well known over the temperature range used in this study. The alloys were all solution treated at 773 K and cooled slowly to room temperature prior to testing.

Fig. 1 shows the grain structure and inclusion distribution at room temperature of the three alloys. The starting average grain size of all the alloys is given in the Table I. The wrought 1100 aluminum alloy contains a distribution of iron-rich inclusions that are relatively large, greater than 1 μm diameter. The wrought- and the P/M-2024 aluminum alloys contain large, 2–3 μm diameter, $CuAl_2$ particles located on the grain boundaries and smaller, less than 1 μm diameter, $CuAl_2$ particles located throughout the interior of the grains. The P/M 2024 alloy also contains oxide inclusions, approximately 3 μm in diameter, that are located along the grain boundaries. These oxides result from the solid-state fabrication process. The chemical composition of these particles was confirmed with analytical scanning electron microscopy.

High-temperature indentation tests were performed, on polished surfaces of each of the three alloys, with a Microtest II micro/nano indentation hardness tester (Micro Materials Ltd., Wrexham, UK) [20–22]. The instrument consists of a vertically mounted ceramic pendulum with a Berkovich diamond indenter attached to the lower end and an electromagnetic actuator attached to the upper end. The actuator causes the pendulum to rotate about a pivot

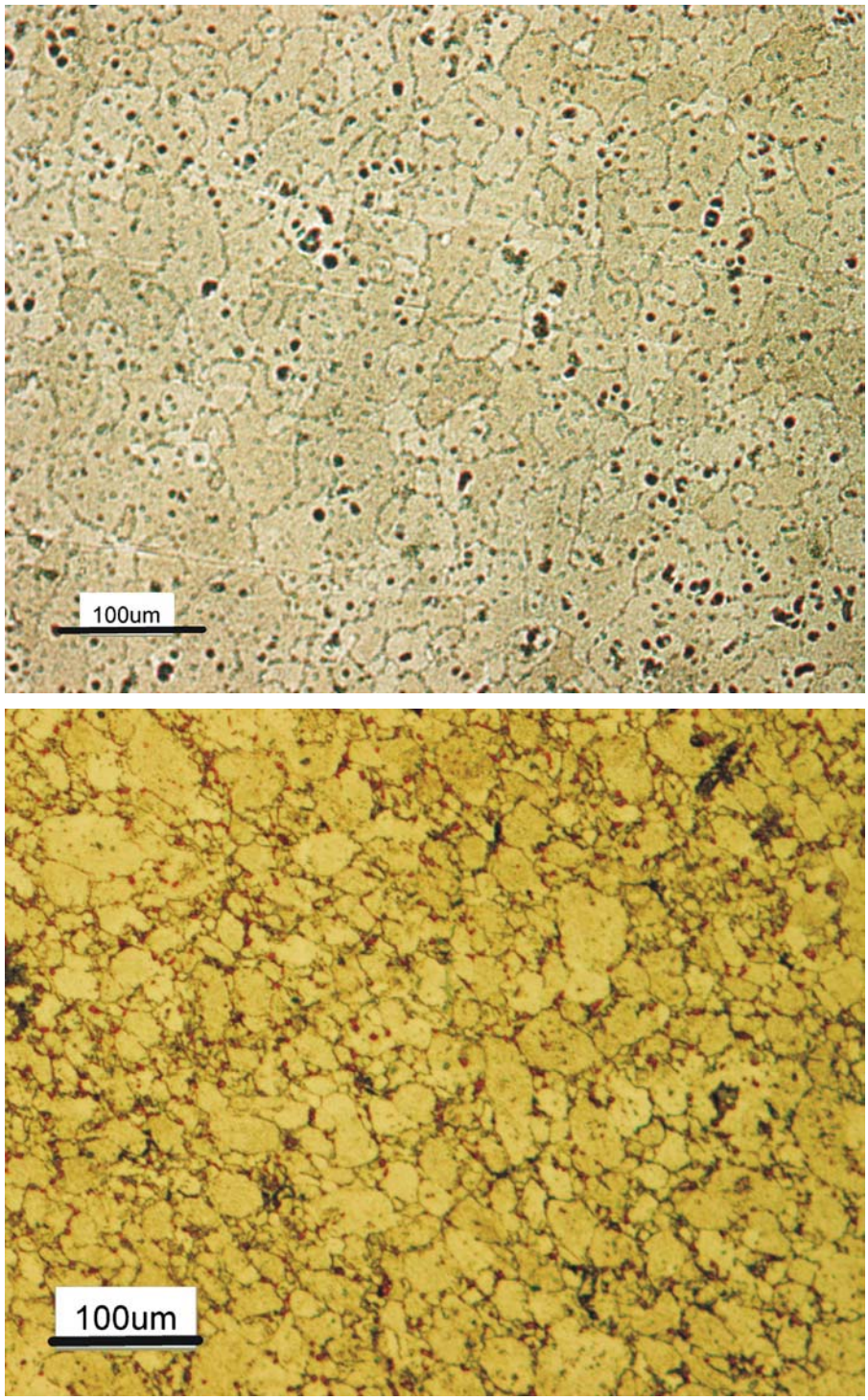

Figure 1 Optical Micrographs of the etched microstructure at room temperature of (a) the wrought 2024 aluminum alloy, (b) the P/M 2024 aluminum alloy, and (c) the wrought 1100 aluminum alloy. All the materials have an average grain size between 10 and 100 μm. The materials all contain inclusions; in the case of the 2024 alloys these inclusion are primarily of $CuAl_2$ composition while, in the case of the 1100 alloy, they are Fe-rich inclusions.

located at its mid-length. A parallel-plate capacitance displacement gauge attached behind the indenter records the indentation depth. The test sample is attached to an electrical heating stage located in front of the indenter. Thermal insulation surrounds the indenter and the specimen. The instrument is located in a temperature-controlled cabinet that rests upon an air table. A mildly reducing atmosphere of Ar-2% H_2 is maintained within the cabinet during the indentation tests to limit oxidation of the sample.

Between 8 and 20 constant-load indentation tests were performed on each alloys at each of the test temperatures. The two 2024 aluminum alloys were tested at 473, 573, 673, 773, and 833 K. This spans the temperature range up to the solidus temperature including the single-α phase and the two-phase α + $CuAl_2$ regions.

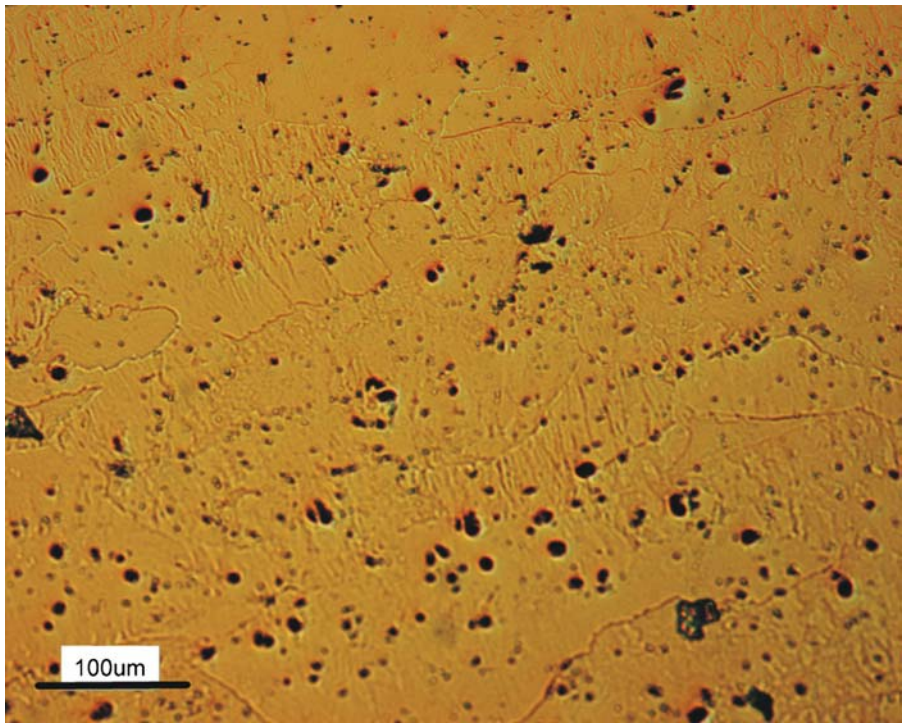

Figure 1 Continued.

The 1100 aluminum alloy is in the single-α phase at all temperatures up to the melting temperature and indentation tests were therefore only performed at 573, 673, and 773 K.

The indentation tests were all performed in order of ascending temperature and the samples were not cooled between testing at each temperature. The samples were held at each temperature for approximately five hours in

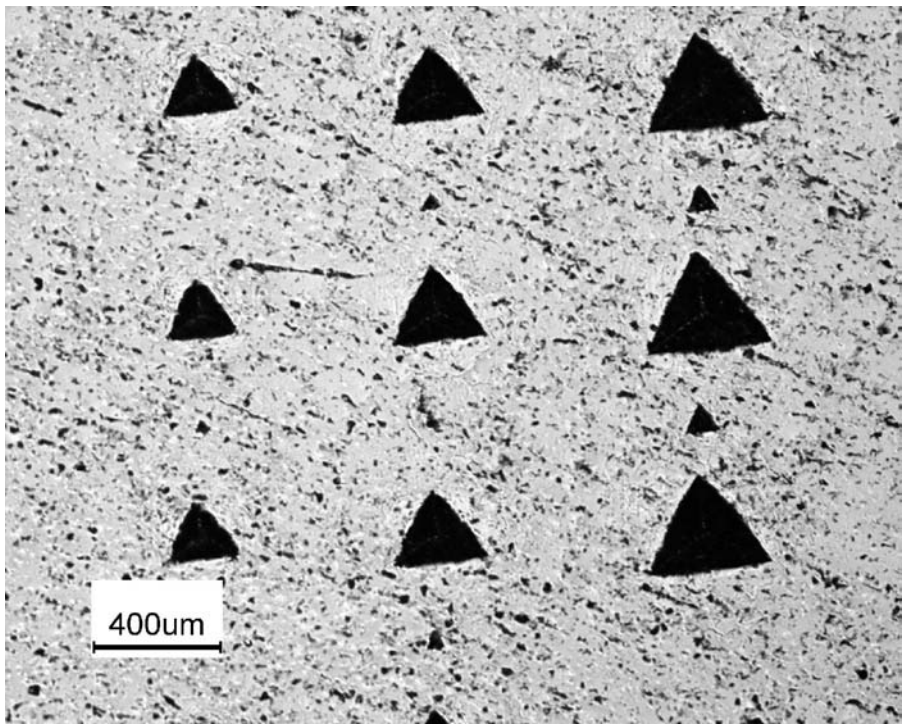

Figure 2 Optical micrograph of several indentations made on the wrought 1100 aluminum alloy. The left-most column of indentations was made at 573 K, the middle column was made at 673 K, and the right-most column was made at 773 K. The indentations made at the higher temperatures are larger because the indentation strain rate was higher during the 100 s constant load period of these tests. The small indentations located between the large indentations were made by the indenter to locate the surface of the test material.

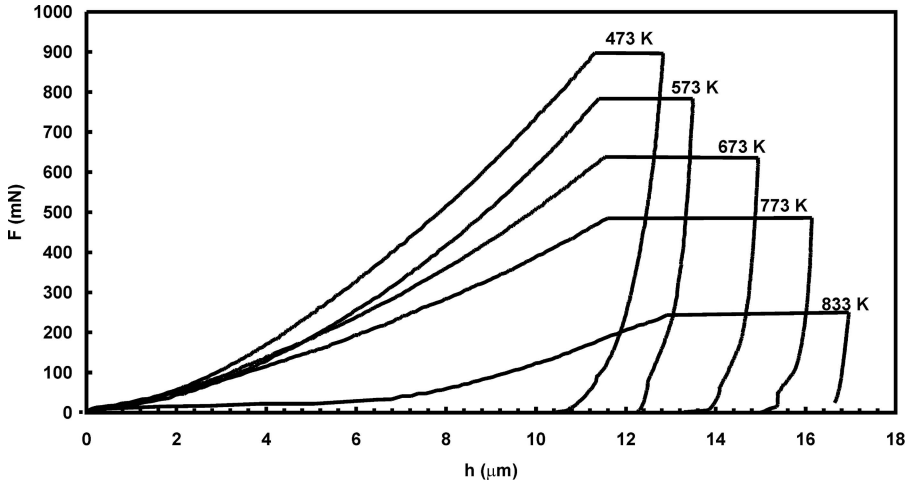

Figure 3 Indentation force F versus indentation depth h of an indentation made, on the P/M 2024 aluminum alloy, at each of the five test temperatures. The curves indicate the softening of the test material with increasing temperature. The horizontal section of each curve indicates the change in h resulting during the 100 s constant load period of the tests.

order to achieve thermal equilibrium before indentation tests commenced.

Each indentation test began with the application of the indentation force at a rate of 50 mN/s until an indentation depth of between 11 and 13 μm was attained. The indentation load was then held constant for 100 s during which time the indentation depth was recorded at half-second intervals. All indentation depth data were corrected for the effects of thermal drift in the indentation depth signal and load frame compliance. Fig. 2 shows indentations made at 573 K, 673 K, and 773 K on the wrought 1100 aluminum alloy. The indentations all showed small amounts of metal pileup which became visible only at a higher magnification than that in Fig. 2. The curvature of the indentation edges that results from metal pileup remained approximately constant, relative to the length of the indentation edge, at all the temperatures tested.

3. Results

Typical data obtained from the indentation creep tests are shown in Figs. 3 and 4 where the results from one test performed on the P/M 2024 aluminum alloy at each of the five test temperatures are depicted. The indentation force F is plotted versus indentation depth h in Fig. 3 while Fig. 4 shows h versus time t during the constant F segment of the tests.

Fig. 5 indicates $\dot{\varepsilon}_{\text{ind}}$ versus $\sigma_{\text{ind}} = F/24.5\,h^2$ for the tests shown in Figs. 3 and 4. The indentation threshold stress

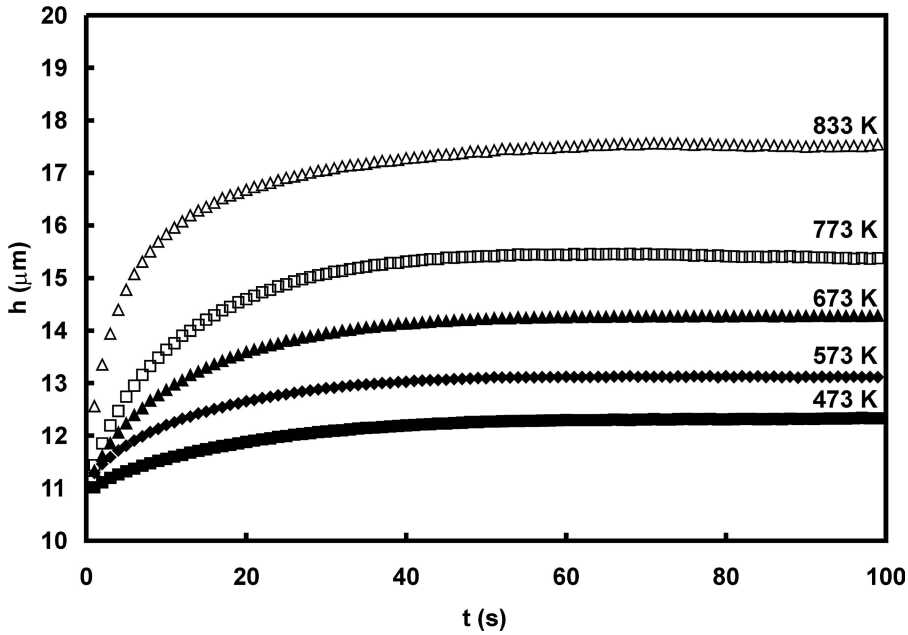

Figure 4 Indentation depth h versus time t during the 100 s constant load segment of the indentation tests shown in Fig. 3. The curves indicate the increasing h, resulting from increasing indentation creep, as the test temperature and testing duration increase.

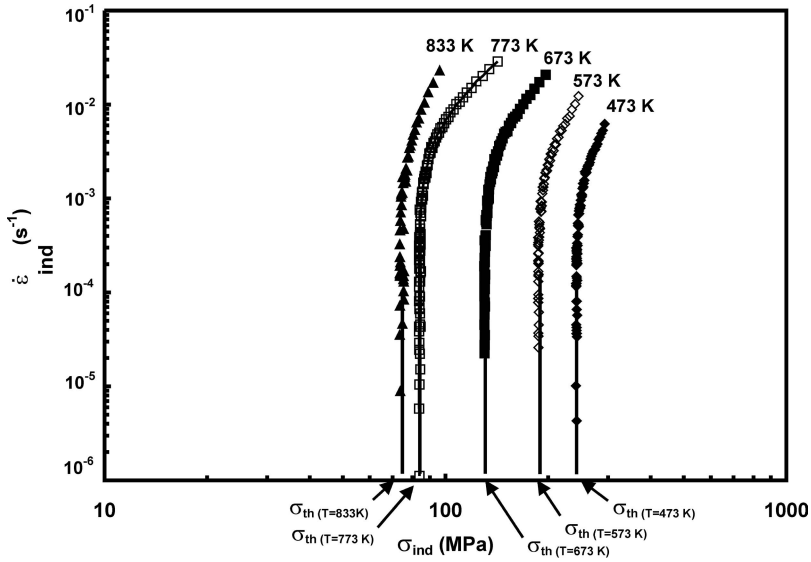

Figure 5 Logarithmic plot of the average indentation strain rate $\dot{\varepsilon}_{ind}$ (Equation 3) versus indentation stress σ_{ind} over the constant load segments of the tests shown in Figs. 3 and 4. The trends shown by the data are extrapolated to determine the threshold stress σ_{th} corresponding to $\dot{\varepsilon}_{ind} = 10^{-6}$ sec.$^{-1}$

σ_{th} was approximated as the stress corresponding to $\dot{\varepsilon}_{ind} = 10^{-6}s^{-1}$. Fig. 6 shows σ_{th}, normalized to the elastic shear modulus μ of pure aluminum, versus T for the three aluminum alloys tested. The following equation was used to calculate μ in units of MPa [14]

$$\mu = 25400\left(1 - \frac{0.5(T - 300)}{933}\right) \tag{4}$$

All the materials display decreasing σ_{th}/μ with increasing temperature. The two 2024 alloys show similar dependence of σ_{th}/μ upon T and their values of σ_{th}/μ are greater, at any given temperature, than that of the wrought 1100 alloy. The variability in σ_{th}/μ for tests performed at the same temperature results from: 1) uncertainty in the extrapolated value of σ_{th} and 2) the non-homogeneous microstructure of the indented material.

The data in Fig. 6 are consistent with the findings reported from previous studies which have shown that a finite σ_{th} is generally present during uniaxial tensile testing of dispersion-strengthened ductile metals, including the 2024 aluminum alloy, and σ_{th}/μ decreases with increasing temperature [23]. The 2024 aluminum alloys show higher values of σ_{th}/μ than the wrought 1100 alloy particularly at the lower temperatures. The 2024 alloys have at higher number of dispersed particles, present as $CuAl_2$ and embedded oxides, in the microstructure compared to the wrought 1100 aluminum alloy. The relationship between σ_{th} and the microstructure of the three alloys is discussed further in Section 4.1.

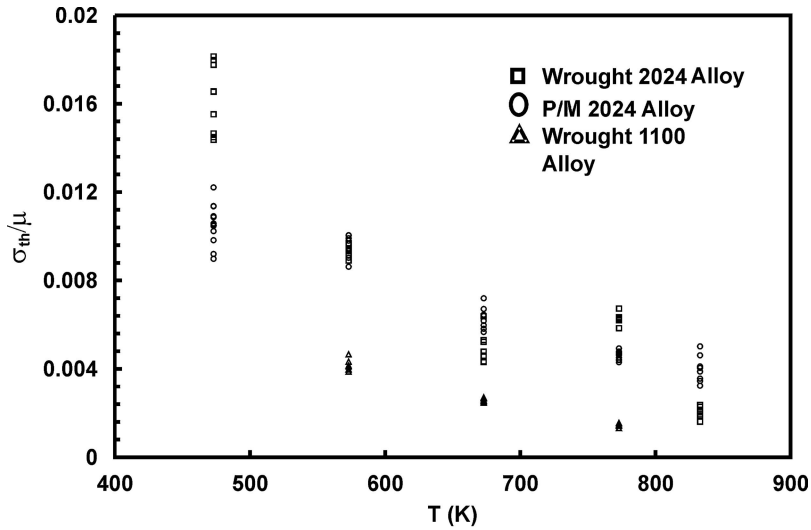

Figure 6 The threshold indentation stress σ_{th}, normalized with respect to the elastic shear modulus μ (Equation 4), versus temperature for all the indentation creep tests performed in this investigation.

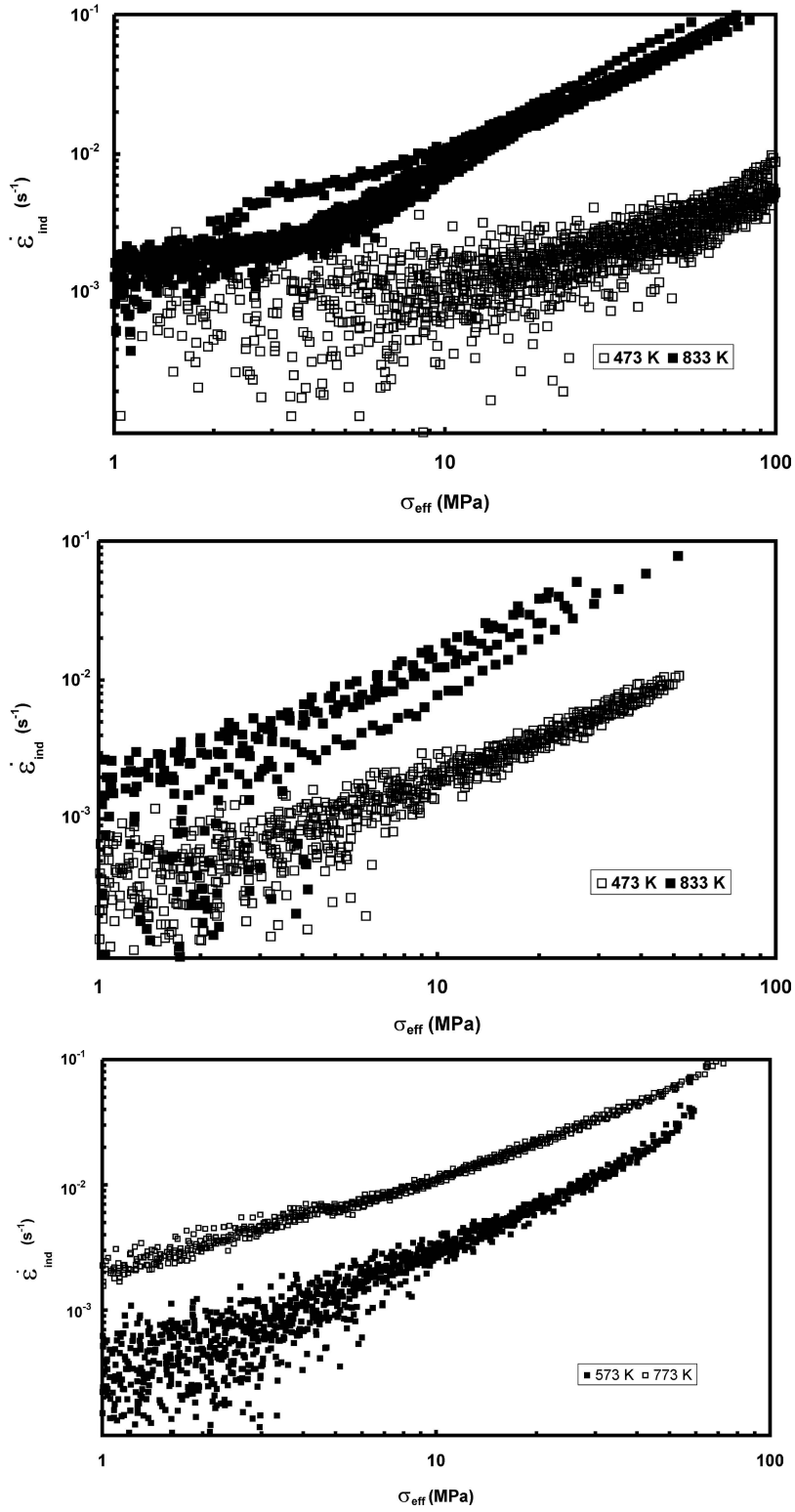

Figure 7 Logarithmic plots of average indentation strain rate $\dot{\varepsilon}_{ind}$ versus effective indentation stress σ_{eff} (Equation 5) for eight indentation creep tests performed at the highest and the lowest temperatures tested for (a) the wrought 2024 aluminum alloy, (b) the P/M 2024 aluminum alloy, and (c) the wrought 1100 aluminum alloy. The curves for all the materials show increased non-linearity at the lower test temperatures.

The presence of a measurable σ_{th} for all the aluminum alloys indicates that $\dot{\varepsilon}_{ind}$ is driven by an effective indentation stress that can be expressed as

$$\sigma_{eff} = \sigma_{ind} - \sigma_{th} \tag{5}$$

Fig. 7 shows logarithmic plots of $\dot{\varepsilon}_{ind}$ versus σeff for single indentation tests performed at 473 K and 833 K on the two 2024 aluminum alloys and at 573 and 773 K on the wrought 1100 aluminum alloy. These are the upper- and lower-temperature limits of the tests

performed in this study. The materials all show nonlinear logarithmic trends of $\dot{\varepsilon}_{ind}$ versus σ_{eff} eff with the degree of non-linearity increasing as T decreases. While $\dot{\varepsilon}_{ind}$ is of the same order of magnitude as the steady-state strain rate of polycrystalline Al, tested at the same temperatures and levels of effective stress as this study (see Pg. 26 of Reference. 14), the nonlinear logarithmic trends shown in Fig. 7 suggest that a steady-state microstructure does not exist during the indentation tests. This is particularly true at the lower temperatures when the trend of the log ($\dot{\varepsilon}_{ind}$) versus log (σ_{eff}) is clearly nonlinear. This fundamental difference precludes detailed comparison of the stress- and temperature-dependence of $\dot{\varepsilon}_{ind}$ with previously reported steady-state creep rate data.

4. Discussion

The results presented above indicate that differences exist in the magnitude of σ_{th} and the dependence of $\dot{\varepsilon}_{ind}$ upon eff for the three aluminum alloys tested. The data also suggest that steady-state deformation does not exist during these indentation tests, particularly at the lower temperatures. We now calculate the nominal inter-obstacle spacing ℓ^* from the measured σ_{th} and evaluate the activation energy ΔG_o of the deformation rate controlling obstacles at the point when σ_{th} occurs. These parameters approximate those related to the steady-state microstructure in the indentation plastic zone of the materials since $\dot{\varepsilon}_{ind}$ is very small, and no longer changing rapidly, when σ_{th} is measured at the end of each test. We discuss the temperature-dependence of ℓ^* and ΔG_o and compare the values amongst the three alloys. We attempt to demonstrate that the changes in these parameters with temperature reflect the known changes in the microstructure of the three aluminum alloys.

4.1. The nominal inter-obstacle spacing ℓ^*

Since all the indentation creep tests were performed with the same, geometrically self-similar, Berkovich indenter at approximately the same indentation depth ($h = 11$ to 13 μm), the average strain state beneath the indenter, at any given temperature, will be quite similar for all the tests. Under these conditions, differences in σ_{th} from one alloy to another reflect differences in the microstructure of the indented materials. If one considers the operative dislocation-obstacle interaction to involve some variation of the mechanism of Orowan bowing of dislocations between rigid obstacles, the inter-obstacle spacing ℓ will be inversely related to σ_{th} and can be expressed as

$$\ell = Ab\frac{\mu}{\sigma_{th}} \tag{6}$$

where A is a constant and b is the Burgers vector. The magnitude of A is not known since it will depend upon the indenter geometry. We therefore assign $A = 1$ for all the materials tested and refer to ℓ^* as the "nominal" inter-obstacle spacing ℓ^*.

The nominal inter-obstacle spacing is plotted versus temperature in Fig. 8. Both 2024 aluminum alloys display similar trends ℓ^* of with T; ℓ^* increases slowly from 0.02 to 0.07 μm with increasing temperature from 473 to 773 K, and then increases rapidly to about 0.15 μm for the wrought 2024 alloy, but continues to increase slowly to 0.08 μm for the P/M 2024 alloy, at 833 K. These variations in ℓ^* are consistent with the phases that are present over this temperature range in the 2024 aluminum alloy. The small increase in ℓ^* with temperature from 473 to 773 K corresponds to decreasing amounts of $CuAl_2$ precipitates in the alloy as the temperature raises through the $\alpha + CuAl_2$ two-phase region. The more rapid increase in ℓ^* from 773 K to 833 K for the wrought 2024 alloy corresponds to the region where the alloy is in the single phase condition. Although no $CuAl_2$ precipitates are present in either 2024 alloy above 773 K, other particles, such as oxides, may be present in the P/M 2024 alloy. This is consistent with the data shown in Fig. 8 that indicate that ℓ^* is considerably less at 833 K for the P/M 2024 than for the wrought 2024 aluminum alloy. The P/M fabricated alloy is expected to have a significantly higher

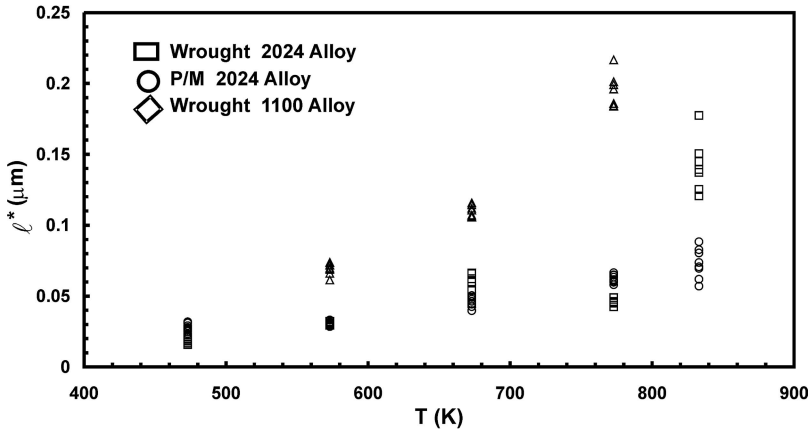

Figure 8 Nominal inter-particle spacing ℓ^* (Equation 7) versus temperature for all the indentation creep tests performed in this investigation.

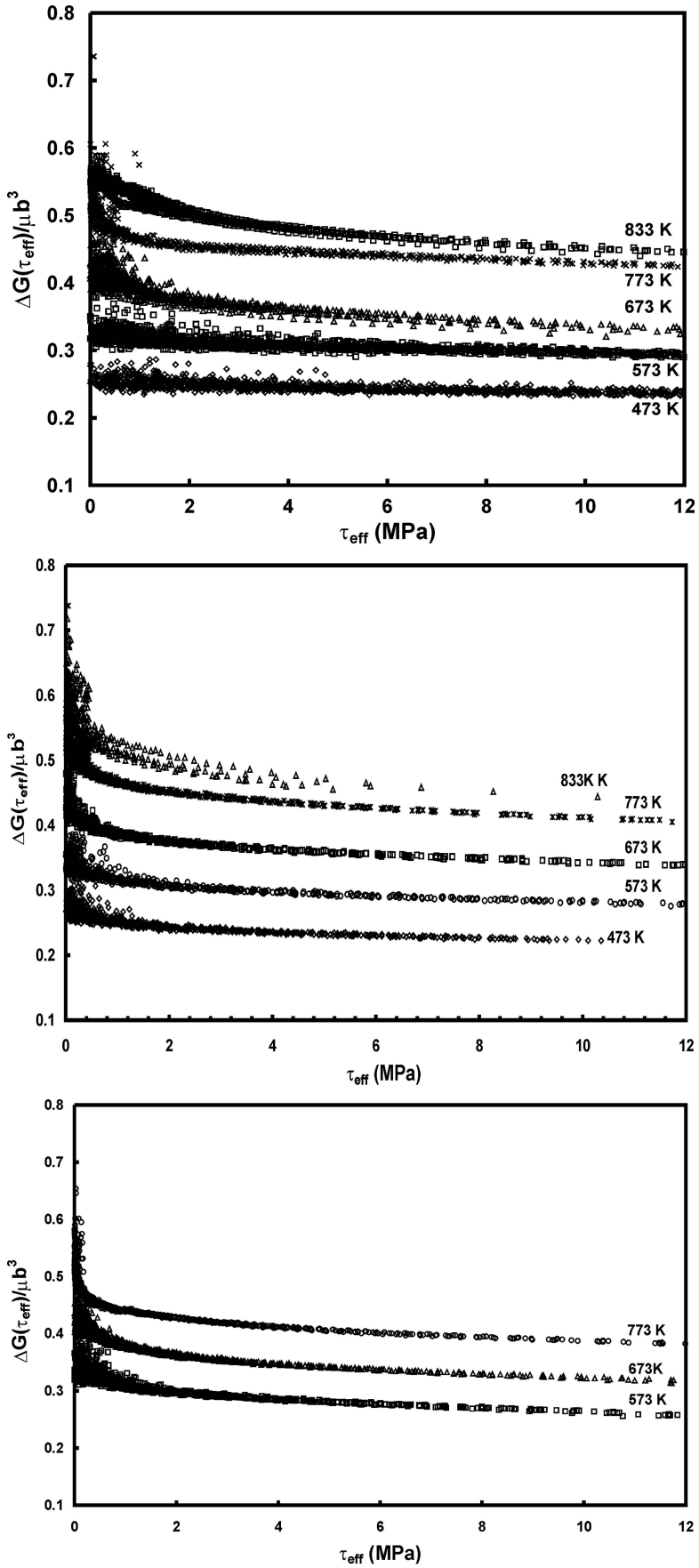

Figure 9 Apparent thermal activation energy $\Delta G(\tau_{\text{eff}})$ (Equation 1), normalized with respect to strain energy of a dislocation, μb^3 versus the effective indentation shear stress τ_{eff} (Equation 2) for the indentation tests performed on (a) the wrought 2024 aluminum alloy, (b) the P/M 2024 aluminum alloy, and (c) the wrought 1100 aluminum alloy.

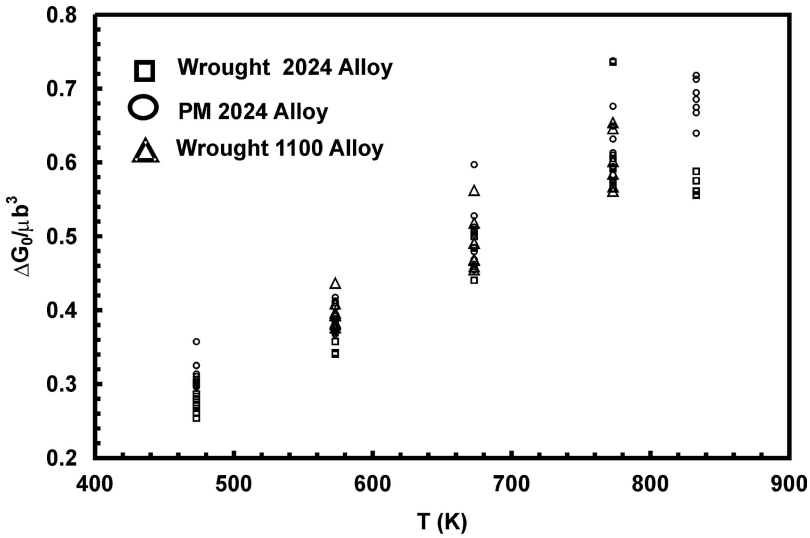

Figure 10 The normalized activation energy $\Delta G_o/\mu b^3$ at $\tau_{eff} = 0$, determined from the data in Fig. 9, versus temperature for all the indentation creep tests performed in this investigation.

concentration of oxides in the microstructure, compared to the wrought alloy, as a result of the solid-state fabrication process [24].

The nominal inter-obstacle spacing of the wrought 1100 aluminum alloy is larger at all the temperatures than it is in either 2024 alloy (Fig. 8). The 1100 alloy has a single-α phase microstructure at all the test temperatures with a distribution of large iron-bearing inclusions (Fig. 1). Since the size and spacing of these inclusions is not expected to change significantly with temperature, we suggest that the increase in ℓ^* with temperature indicates that the deformation rate limiting obstacles in the wrought 1100 aluminum alloy are not particles but rather dislocation structures, grain boundaries or sub-grain boundaries whose spacing increases with temperature due to thermal recovery and recrystallization.

Although the above analysis is based upon a simplistic Orowan bowing dislocation/obstacle interaction mechanism, it indicates that the σ_{th} determined from high-temperature constant-load indentation testing is sufficiently precise to discern differences in obstacle spacing between the three aluminum alloys and these differences are consistent with what is known of the particle distributions within the alloys.

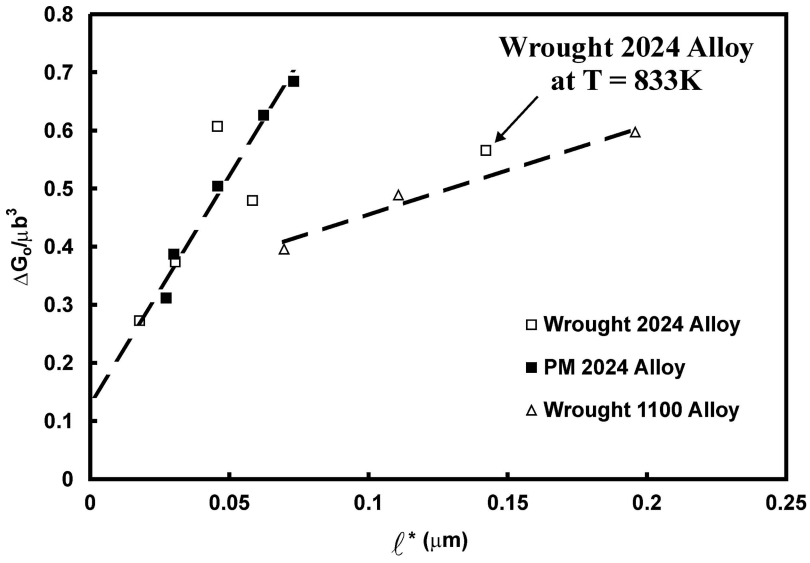

Figure 11 The normalized activation energy $\Delta G_0/\mu b^3$ at $\tau_{eff} = 0$ versus nominal inter-obstacle spacing ℓ^* for all the indentation creep tests performed in this investigation. At temperature up to 773 K, both 2024 aluminum alloys follow the same trend of increasing $\Delta G_0/\mu b^3$ with temperature which is different than that followed by the 1100 aluminum alloy. The 2024 alloy is in the two-phase microstructural regime over this temperature range. At 833 K, the data from the wrought 2024 aluminum alloy falls upon the curve described by the 1100 alloy indicating that the $CuAl_2$ particles have dissolved leaving a single-phase α microstructure. The P/M 2024 aluminum alloy continues to follow the trend described by both 2024 alloys at the lower temperatures indicating that significant amounts of oxide particles are still present at 833 K to act as obstacles to dislocation glide.

4.2. The activation energy ΔG_o of the deformation rate-controlling obstacles

When σ_{ind} is greater than σ_{th}, obstacle-limited dislocation glide occurs and the dependence of γ_{ind} upon τ_{eff} and T is given by Equation 1. We apply this equation, and Equations. 2 and 3, to the $\dot{\varepsilon}_{ind}$ versus σ_{eff} data from the tests to construct plots of $\Delta G(\tau_{eff})$ versus τ_{eff} for each test (Fig. 9). The $\Delta G(\tau_{eff})$ versus τ_{eff} trends indicate that the strength of the dislocation-obstacle interactions that control $\dot{\varepsilon}_{ind}$ change during the course of the constant load indentation tests. $\sigma G(\tau_{eff})$ is very small in the early stages of the test when τ_{eff} is large but increases in magnitude as the test progresses. The fact that $\Delta G(\tau_{eff})$ is not constant during the test is further evidence that a steady-state microstructure does not exist around the indentations. The data in Fig. 9 describe the evolution of the microstructure during the specific indentation tests. The shapes of the trends in this figure are not a unique material property; they depends upon a variety of parameters including the initial indentation loading rate. The value of ΔG at $\tau_{eff} = 0$ will converge, however, to a constant value which is the apparent activation energy ΔG_o of the deformation rate-controlling obstacles under steady-state conditions.

Fig, 10 shows $\Delta G_o/\mu b^3$ versus T. The three aluminum alloys tested all show the same trend of increasing ΔG_o with increasing T. ΔG_o ranges from 0.30 to 0.65 μb^3 and is, therefore, well within the range of the activation energy for "medium strength" obstacles such as weak particles or dislocation/dislocation interactions [14].

We have presented, in the sections above, analyses of both σ_{th} and $\dot{\varepsilon}_{ind}$ in terms of mechanisms involving obstacle-limited dislocation glide. Our data suggest that σ_{th}, for the case of the 2024 alloys, is a function of the spacing of $CuAl_2$ and oxide particles while for the 1100 alloy it is a function of the average dislocation network spacing. When an indentation stress greater than σ_{th} is applied, time-dependant deformation occurs and the magnitude of $\dot{\varepsilon}_{ind}$ is a function of the strength, ΔG, of the obstacles. The fact that ΔG changes with time during the constant-load indentation tests, but the value of ΔG_o is always between 0.30 to 0.65 μb_3, suggests that ΔG is related to a dislocation — type of obstacle whose size, and strength, changes during the course of the test. It is reasonable to assume that ΔG_o and ℓ arise from the same obstacles. This is discussed below.

Plotting $\Delta G_0/\mu b^3$ versus ℓ (Fig. 11) indicates a clear difference in the dependence ΔG_0 of upon the apparent inter-obstacle spacing for the 2024 aluminum alloys compared to the wrought 1100 alloy. At temperature less than 773 K, both 2024 aluminum alloys follow the same linear relationship of increasing ΔG_o with increasing ℓ and this trend is distinctly different than the one displayed by the 1100 aluminum alloy. This difference can be explained in terms of the presence of $CuAl_2$ and oxide particles in the 2024 aluminum alloy which provide obstacles of about the same strength but spaced closer together than what are found in the wrought 1100 aluminum alloy. At 833 K, when the $CuAl_2$ particles are no longer present, the wrought 2024 aluminum alloy shows a $\Delta G_o/\mu b^3$ versus ℓ relationship that falls upon the trend described by the wrought 1100 aluminum alloy while the P/M 2024 aluminum alloy continues to follow the linear trend shown by both 2024 alloys at the lower temperatures. This suggests that the large number of oxides present in the P/M 2024 alloy continue to provide effective obstacles to dislocation glide at 833 K.

The analyses of ℓ^* and ΔG_0 described above does not account for the possible contribution of deformation mechanisms that cannot be described by Equation 1. It is very likely that interfacial sliding contributes to the deformation rate at 833 K [8, 25–28]. Inclusion of this mechanism into the analysis of the data is currently being studied.

5. Conclusions

The results of this investigation have shown that constant-load, short-time duration, pyramidal indentation testing is sufficiently precise to detect the temperature dependence of fundamental deformation parameters, such as ℓ^* and ΔG_0, of three common aluminum alloys. The primary findings are summarized below.

The average indentation strain rate $\dot{\varepsilon}_{ind}$ of the three alloys tested all show threshold stress σ_{th} that decreases with increasing temperature. The temperature-dependence of the nominal inter-obstacle spacing ℓ^*, calculated from σ_{th}, is different for the three alloys. In the case of the wrought- and the P/M-fabricated 2024 aluminum alloys, the increase in ℓ^* with temperature from 473 K to 773 K is consistent with the known temperature-dependent change in the amount of $CuAl_2$ precipitates. increases considerably at 833 K for the wrought 2024 alloy but remains low for the P/M 2024 alloy. This indicates that the presence of oxides within the P/M 2024 material continues to limit the deformation rates of the material at temperatures when the $CuAl_2$ precipitates have dissolved.

The wrought 1100 aluminum alloy shows steadily increasing ℓ^* with increasing temperature even though the spacing of the inclusions in this alloy is not expected to change with temperature. We suggest, therefore, that the measured σ_{th} is the result of dislocation/dislocation interactions, whose spacing does increase with temperature.

The three alloys all show non-linear logarithmic dependencies of $\dot{\varepsilon}_{ind}$ upon σ_{eff} and the degree of non-linearity increases with decreasing temperature. This indicates that the microstructure is changing, and steady-state conditions don't exist, within the indentation plastic zone during the course of the tests. The calculated activation energy ΔG_0 of the deformation rate at the end of the constant-load indentation test, when $\dot{\varepsilon}_{ind}$ is small and no longer changing rapidly, is approximately 0.30 μb^3 at 473 K and increases to 0.65 μb^3 at 833 K

for the alloys tested. These values are well within the range of activation energy of "medium strength" obstacles such as weak particles or dislocation/dislocation interactions.

At temperatures between 473 and 773 K, both 2024 aluminum alloys follow the same linear relationship of $\Delta G_0/\mu b^3$ versus ℓ^*. This relationship is clearly different than the linear $\Delta G_0/\mu b^3$ versus ℓ^* relationship displayed by the 1100 aluminum alloy. The ΔG_0 is higher, for a given ℓ^*, in this temperature range for the 2024 alloys than it was for the 1100 aluminum alloy. This is consistent with the fact that the 2024 aluminum alloy contains more particles, $CuAl_2$ precipitates, which, while being of approximately the same strength as the obstacles found in the 1100 alloy, are spaced more closely together. At 833 K, the $CuAl_2$ precipitates are dissolved and $\Delta G_0/\mu b^3$ of the wrought 2024 aluminum alloy falls upon the trend of $\Delta G_0/\mu b^3$ versus described by the wrought 1100 alloy while the P/M 2024 aluminum alloy continues to follow the same $\Delta G_0/\mu b^3$ versus ℓ^* trend displayed by both 2024 alloys at lower temperatures. This suggests that the distribution of oxides in the P/M 2024 alloy continue to limit the indentation deformation rate at 833 K.

This study has demonstrated that short duration constant-load microindentation testing performed at elevated temperatures using modern computer-controlled equipment is sufficiently precise to detect differences in the indentation strain rate that are related to microstructural differences between different alloys of similar base-composition.

Acknowledgments

The authors wish to thank Mr. R.N. Saraf for fabricating the aluminum alloy samples used in this study and the Natural Science and Engineering Research Council of Canada who provided financial support for this research.

References

1. J. POMEY, A. ROYEZ and J. P. GEORGES, *Rev. Met.* **56** (1959) 215.
2. T. O. MULHEARN and D. TABOR, *J. Inst. Metals* **89** (1960) 7.
3. A. G. ATKINS, A. SILVÉRIO and D. TABOR, *J. Inst. Met.* **94** (1966) 369.
4. C. J. FAIRBANKS, R. S. POLVANI, S. M. WEIDERHORN, B. J. HOCKEY and B. R. LAWN, *J. Mater. Sci. Lett.* **1** (1982) 391.
5. P. M. SARGENT and M. F. ASHBY, *Mater. Sci. Technol.* **8** (1992) 594
6. W. B. LI, J. L. HENSHALL, R. M. HOOPER and K. E. EASTERLING, *Acta Metall. Mater.* **39** (1991) 3099.
7. B. N. LUCAS and W. C. OLIVER, *Metall. Mater. Trans.* A **30** (1999) 601.
8. M. J. MAYO and W. D. NIX, *Acta Metall.* **36** (1988) 2183.
9. T. P. WEIHS and J. B. PETHICA, *Mater. Res. Soc. Symp. Proc.* **239** (1992) 325.
10. V. RAMAN and R. BERRICHE, *J. Mater. Res.* **7** (1992) 627.
11. B. N. LUCAS and W. C. OLIVER, *Mater. Res. Soc. Symp. Proc.* **239** (1992) 337.
12. S. P. BAKER, T. W. BARBEE and W. D. NIX, *Mater. Res. Soc. Symp. Proc.* **239** (1992) 319.
13. G. FENG and A. H. W. NGAN, *Scripta Mater.* **45** (2001) 971.
14. H. J. FROST and M. F. ASHBY, "Deformation-Mechanism Maps" (Pergamon Press, Oxford, 1982) p.21.
15. S. SAIMOTO, B. J. DIAK and K. R. UPADHYAYA, *Mater. Sci. Engng.* **A234 – 236** (1997) 1015.
16. B. J. DK and S. SAIMOTO, *Mater. Sci. Engng.* **A319 – 321** (2001) 909.
17. A. A. ELMUSTAFA and D. S. STONE, *J. Mech. Phys. Solids* **51** (2003) 357.
18. R. J. KLASSEN, B. J. DIAK and S. SAIMOTO, *Mater. Sci. Engng.* **A387 - 389** (2004) 297.
19. R. N. SARAF, M.E. Sc "Creep Behaviour of Al-Based Composites Made By The P/M Technique" Thesis University of Western Ontario, London Canada, 2002.
20. J. F. SMITH and S. ZHANG, *Surf. Engng.* **16** (2000) 143.
21. B. D. BEAKE and J. F. SMITH, *Philos. Mag.* **A8** (2002) 2179.
22. B. D. BEAKE, S. R. GOODES, J. F. SMITH and Z. METALLKD **7** (2003) 798.
23. J. C. GIBELING and W. D. NIX, *Mater. Sci. Engng.* **45** (1980) 123.
24. F. A. MOHAMED, *Mater. Sci. Engng.* **A245** (1998) 242.
25. S. R. NUTT and R. W. CARPENTER, *Mater. Sci. Eng.* **75** (1985) 169.
26. M. STRANGWOOD, C. A. HIPPSLEY and J. J. LEWANDOWSKI, *Scripta Metal. et Mater.* **24** (1990) 1483.
27. W.-J. KIM and O. D. SHERBY, *Acta Mater.* **48** (2000) 1763.
28. W.-J. KIM, D.-W. KUM and H.-G. JEONG, *J. Mater. Res.* **16** (2001) 2429.

Received 19 April
and accepted 27 June 2005